Interpretation®

Geometric Seismic Attribute Estimation using Data-adaptive Windows

Journal:	*Interpretation*
Manuscript ID	INT-2018-0114.R1
Manuscript Type:	2018-02 Seismic geometric attributes
Date Submitted by the Author:	04-Nov-2018
Complete List of Authors:	Lin, Tengfei; Research Institute of Petroleum Exploration and Development, PetroChina, Department of Middle East E&P; University of Oklahoma, School of Geology and Geophysics Zhang, Bo; The University of Alabama, Geological Sciences Marfurt, Kurt; Oklahoma University, School of Geology and Geophysics
Keywords:	seismic attributes, North America, 3D
Subject Areas:	Structural, stratigraphic, and sedimentologic interpretation, Interpretation concepts, algorithms, methods, and tools

Geometric Seismic Attribute Estimation using Data-adaptive Windows

Tengfei Lin[1], Bo Zhang[2], Kurt Marfurt[3]

[1] Department of Middle East E&P, Research Institute of Petroleum Exploration & Development, PetroChina

[2] University of Alabama, Department of Geological Sciences,

[3] University of Oklahoma, ConocoPhillips School of Geology and Geophysics.

lintf@petrochina.com.cn, bzhang33@ua.edu, kmartfurt@ou.edu,

Corresponding author:

Bo Zhang

University of Alabama, Department of Geological Sciences

7 201 7th Ave.

Room 2003 Bevill Building

Tuscaloosa, AL 35487

bzhang33@ua.edu

ABSTRACT

Geometric seismic attributes such as coherence are routinely used for highlighting the geological features such as faults and channels. Traditionally, we use a single user-defined analysis window of fixed size to calculate attributes for the entire seismic volume. In general, smaller windows produce sharper geological edges but they are more sensitive to noise. In contrast, larger windows reduce the effect of random noise, but might laterally smear faults and channel edges and vertically mix the stratigraphy. The vertical and lateral resolution of a 3D seismic survey changes with depth due to attenuation losses and velocity increase, such that a window size that provides optimal images in the shallower section is often too small for the deeper section. A common workaround to address this problem is to compute the seismic attributes using a suite of fixed windows and then splice the results at the risk of reducing the vertical continuity of the final volume. Our proposed solution is to define laterally and vertical smoothly varying analysis windows. The construction of such tapered windows requires a simple modification of the covariance matrix for eigenstructure-based coherence and a less obvious, but also simple modification of semblance-based coherence. We demonstrate the values of our algorithm by applying it to a vintage 3D seismic survey acquired offshore Louisiana, USA.

LIST OF KEYWORDS

Seismic Attributes, Coherence, Spectral Decomposition, and Resolution.

INTRODUCTION

Geometric seismic attributes such as coherence measure changes in reflector shape and continuity (Chopra and Marfurt 2007) that can be tied to structural features such as faults and sedimentary features such as channel edges. While instantaneous and spectral attributes are computed trace by trace, geometric attributes are computed from a window of neighboring traces and samples. "Coherence" can be computed using cross-correlation (Bahorich and Farmer, 1995), semblance or variance (e.g., Marfurt et al., 1998; Marfurt, 2006; Pepper and Bejarano, 2005), Sobel filters (Luo et al., 1996; Barka, 2015), eigenvectors of the data covariance matrix (Gersztenkorn and Marfurt, 1999), eigenvectors of the gradient structure tensor (van Bemmel and Pepper, 2011), and prediction error filters (Bednar, 1998). Based on the coherence corresponding to the possible faults regions, Wang and Alregib (2017) come up with the interactive fault extraction method by Hough Transform and tracking vectors.

Most implementations of these algorithms use a fixed number of traces and samples for the entire volume to be analyzed. However, due to frequency losses in the overburden, as well as the increase of seismic velocity and decreasing range of incident angles with depth, the seismic data lose both temporal and lateral resolution with depth. Hence, a fixed analysis window optimized for the shallow section might provide suboptimal results in the deeper section. A workaround is to approximate a time-variant algorithm by splicing the results of a suite of coherence computations run with different vertical and lateral window dimensions. Unfortunately, the blended output generally lacks vertical continuity. To address these problems, Barka (2015) defined the vertical

size of a Sobel filter edge detector based on the frequency content. Lin et al. (2014a) showed how smoothed estimates of peak spectral frequency could help to define the data-adaptive vertical analysis windows to compute volumetric dip and coherence.

In this paper, we generalize Lin et al.'s (2014b) data adaptive workflow to define both the vertical and lateral size of the analysis window to be a function of the smoothed local spectral content, where the spectral magnitudes are computed using spectral decomposition. We begin with a review of the sensitivity of the quality of coherence images to analysis window size. Next, we review the computation of energy ratio coherence based on the Karhunen-Loeve (KL) filter (Marfurt et al., 1998; Chopra and Marfurt, 2007) and show its relation to semblance. We then show how to construct the covariance matrix for vertically and radially tapered analysis windows, which in turn provide estimates of coherence. Given these definitions, we apply our modified algorithms to a 3D seismic volume and show the value of using data adaptive windows.

REVIEW-SENSITIVITY OF COHERENCE IMAGES TO WINDOW SIZE

Most geometric attributes including volumetric estimates of dip, coherence, curvature, amplitude gradients, and Gray-Level Co-occurrence Matrix (GLCM) texture are computed within a 3D analysis window that shifts with each voxel analyzed. The lateral and vertical resolution of these attributes are limited by the temporal and spatial sampling intervals, spectral content of the data, and the signal-to-noise ratio. Lin et al. (2016) studied the sensitivity of coherence estimates to random noise using an F-statistic and found that the confidence of finding a coherent event increases with (1) the number of traces, and (2) the product of the bandwidth with vertical window size. Libak et al. (2017) studied the sensitivity of coherence attributes to noise, and analysis window size using both seismic modeling and real data. Since the seismic bandwidth generally decreases with depth, their analysis suggests adaptation of the analysis window size to the spectral content of the seismic data to ensure consistent attribute image quality.

In general, larger analysis windows can reduce random noise and "stack" vertically aligned discontinuities of interest, but will increase computational cost and may smear lateral discontinuities or mix vertical stratigraphy. High frequency data require smaller sampling intervals.

Vertical Mixing of Stratigraphy

To understand the impact of the size of the analysis window on the resulting coherence image, one needs to examine the seismic reflectivity model:

$$d_k = \sum_{m=-M}^{M} \left(r_{k+m} w_m \right) + n_k , \qquad (1)$$

where

d_k is the measured seismic data at the k^{th} sample,

r_k is the reflectivity at the k^{th} sample,

$2M+1$ is the seismic wavelet length; m is the m^{th} value of seismic wavelet,

w_m is a temporally limited seismic wavelet, where $M \leq m \leq M$, and

n_k can be random noise at the k^{th} sample.

The seismic wavelet **w** mixes reflectivity from adjacent depths to the depth of interest. The amount of mixing is a function of the bandwidth of the data. For most seismic surveys, we lose higher frequencies with depth, while the lower frequencies remain, thereby decreasing the bandwidth. For this reason, a reasonable estimate of resolution is the half period (T_{min}, in two- way travel time) or quarter wavelength (λ_{min}, in depth converted data) of the highest useable frequency in the spectrum, while a reasonable estimate of vertical mixing is the dominant period (T_{dom} in two-way travel time) or dominant wavenumber (λ_{dom} in depth converted data). These two numbers provide a means of estimating an optimum analysis window.

Lin et al.'s (2016) work shows that the confidence in coherence estimates for fixed signal-to-noise ratio increases with f_bT, where f_b is the bandwidth measured in Hertz, and T is the temporal analysis window measured in seconds. We therefore expect the imaging quality to improve with increasing window size up to $T=T_{min}$, and improve slightly, but with the risk of mixing, up to $T= T_{dom}$. For values $T> T_{dom}$, any improvement in the signal-to-noise ratio of the image can be offset by increased mixing of geologic features from shallower and deeper events. Marfurt and Alves (2015) described the "false" vertical fabric in mass-transport complex (MTCs) in the southeast Brazil due to the mixed stratigraphy. For these reasons, we hypothesize that analysis windows that adapt to the bandwidth of the data will provide superior, better balanced images than those computed using a fixed window.

Stair-step Artifacts of Dipping Faults

While time slices through coherence volumes provide excellent images of the continuity and orientation of faults, the lateral location of these faults are often shifted from one manually picked on vertical slices through the seismic amplitude data by a human interpreter. Careful examination of vertical slices through the corresponding coherence volume shows the well-known and routinely encountered "stair-step" artifact (Figure 1). Eigenstructure-, semblance-, variance-, and gradient structure tensor based coherence as well as Sobel-filter estimates of discontinuities are dominated by the stronger amplitude events within the analysis window.

Increasing the size of the vertical analysis window beyond the dominant period of a high-amplitude discontinuity undesirably propagates the discontinuity both shallower and deeper within the coherence image. For listric faults, these artifacts become worse than the annoying stair step artifacts, such that the discontinuities of a given fault may appear more than once on time slice (Marfurt and Alves, 2015).

We evaluated two remedies to this problem, neither of which worked. First, we balanced the amplitude of each sample vector within the analysis window to have approximately the same contribution. Such balancing reduced, but did not eliminate the contribution of the stronger discontinuities within the analysis window. Second, we reduced the vertical size of the analysis window. As shown in Figure 1a, even a window size of 1 sample results in a stair-step artifact, suggesting that the artifact is due to the seismic amplitude data and not to the size of the coherence window.

Reflectivity, Seismic Imaging, and the Seismic Wavelet

The stair-step artifact has perplexed the last author of this article since the inception of coherence some 20 years ago. The typical migration algorithm assumes that each subsurface image point is a point diffractor, those algorithms that explicitly include an obliquity factor actually assume each subsurface point is part of a specular reflector. In prestack migration, the obliquity factor is a function of the unit vector from the source to the image point, $\mathbf{p}_s$, the unit vector from the image point to the receiver group, $\mathbf{p}_g$, and the normal to the hypothesized reflector, **n** (Figure 2). In diffraction imaging, one computes **n,** defining the normal to the reflector dip, from a previous image of specular (or conventional) imaging. In this case, the obliquity factor, Ω, is

$$\Omega = \frac{\mathbf{p_s} + \mathbf{p_g}}{2} \cdot \mathbf{n} \ , \tag{2}$$

which geometrically is the cosine of the angle between the average of the angle of incidence and reflection and the normal. Examination of Figure 2 shows that for specular reflection, the angle of incidence equals the angle of reflection about the normal, such that $\Omega = 1$. Furthermore, migration ray pairs, $\mathbf{p_s}$ and $\mathbf{p_g}$, skewed to the left of the specular angle will generally be accompanied by migration ray pairs skewed to the right. In most migration algorithms, the seismic image is built up point diffractor by point diffractor. The net result is that the seismic wavelet will be oriented perpendicular to the reflector, parallel to **n**.

Since this phenomenon is not well recognized by most interpreters, we designed a simple 2D reflectivity model using Tesseral 2D, showing faults with dips of 50°, 60°, 70°, and 80° (Figure 3a). The shot interval is 20 m, receiver interval is 10 m, and the wavelet is Ricker wavelet (40 Hz). Synthetics were generated using a 2D-2C elastic wave equation modeling algorithm. Then we obtain the imaging results by prestack time imaging and prestack depth imaging, and then compute their coherence, respectively (Figures 3b and 3d). Note that the seismic wavelets near the fault edges are aligned perpendicular to the horizontal reflectors. Since these terminations occur at discrete layer boundaries, the result is a discrete stair step, with the vertical extent of the stair step defined by the size of the seismic wavelet.

ATTRIBUTE COMPUTATION USING ADAPTIVE WINDOWS

The above observations suggest that for a fixed signal-to-noise ratio that the ideal analysis window should be a function of the local seismic spectrum (the reciprocal of dominant frequent). Figure 4 is a cartoon showing how the input amplitude data are weighted both vertically and radially from the center. Ideally, smaller window size can be applied to the thinner uniform layers (Figure 4a); and larger window size to the thicker uniform layers (Figure 4b). While it is hard to choose an ultimate window for thick-various laters (Figure 4c). We will apply median filter to smooth our spectra to estimate λ_{dom} and λ_{min} defined above. Furthermore, we will assume our data have been depth converted, through either depth migration or a simple velocity conversion. Finally, since we are as concerned about lateral resolution and mixing as well as vertical resolution and mixing, our analysis windows will vary both vertically and laterally, where "lateral" is defined as parallel to the local structural dip.

APPLICATIONS

We apply our data-adaptive coherence algorithm on a time-migrated data volume from the Gulf of Mexico. The interval sample is 2 ms, and both the inline and crossline spacing are 110 ft. The 3D seismic data (Figure 5a) have been spectrally balanced and subjected to structure-oriented filtering to further improve the vertical and lateral resolution (Figure 5b). Red arrows of the vertical slice in Figures 5a and 5b indicate four faults cutting from them shallower to the deeper section; the wavelength increases with depth as well. The frequency spectra in Figures 6a and 6b, respectively, ranges between 10 to 80 Hz, with a bandwidth that due to attenuation to range between 10~40 Hz.

Figures 7a-d show slices through energy ratio coherence using four different window sizes. Note higher volumes computed resolution in the shallower zone ($t = 0.96$ s), which allows for a smaller window size (Figure 7a). In Figure 7c events at $t = 0.96$ s mix together due to the longer window (40 ms), making it harder to characterize faults and channel edges in the shallower section. In contrast, a larger window should be applied in the deeper section, to generate a more continuous, though lower resolution fault anomalies. The fault in the red dashed rectangular window shows the improvements of fault imaging gradually in Figures 7b and 7c, despite the horizontal blur. Calculations using smoothly tapered data-adaptive windows provide a sharper and cleaner fault imaging in both shallower and deeper sections (Figure 7d).

Figure 8 indicates the zoomed in section of seismic profile of Figure 5b showing Horizon A1 and several normal faults. Figure 9 shows a time-structure ma of Horizon A1 along with a horizon slice through the coherence volume. Normal faults are picked by red lines in the profile, which are crossed by Horizon A1. Figure 9b gives us the seismic amplitude values along Horizon A1, which is located in the trough of the seismic waveform. Several normal faults are indicated by red arrows.

Energy ratio similarity is calculated in Figures 10a-d, using $\pm$ 4 ms, $\pm$ 20 ms, $\pm$ 40 ms and 5 traces, and data-adaptive (varying between $\pm$ 12 ms and 5 traces, and $\pm$ 100 ms and 13 traces) window size, resulting in fault and channel images with different resolution. Smaller windows ($\pm$ 4 ms) suffer from more random noise. Larger windows ($\pm$ 40 ms) suppress thin noise.

Figures 11-16 indicate the phantom horizons, which are 8 ms, 24 ms and 40 ms above Horizon A1. The coherence are calculated by $\pm$ 4 ms, $\pm$ 20 ms, $\pm$ 40 ms and data-adaptive ($\pm$ 12~100 ms) window size. The structural anomalies indicated by white arrow 2 are detected in Figures 10a-10d, and disappears in Figure 14a as it reaches the phantom 24 ms below Horizon A1. While it shows up again in Figure 12c, this is because the large window size ($\pm$ 40 ms) combines too much geological information together and smears the channel edges, making them hard to separate. The approximate dominant frequency nearby Horizon A1 is 20 Hz, and its relevant window size in coherence algorithm is 25 ms, a little larger than the average window size applied in the whole survey. Therefore, the coherence using data-adaptive window gives us perfect results, less random noise, sharper fault anomalies and reduced leakage.

CONCLUSIONS

The "optimum" window height for attributes such as coherence is a function of the dominant period in the window. In general, the analysis window used in geometric attribute calculation should be large enough to improve the signal-to-noise ratio of the estimate, yet small enough to avoid mixing the seismic signal of adjacent stratigraphy or discontinuities. In general, the computational cost of these attributes, as well as all coherence algorithms, increases linearly with the window height and with the square of the its radius. However, the reduction in interpretation time owing to the improved quality of the results compensates for the increased computational time.

Since the seismic amplitude response is the convolution of the reflectivity with the seismic wavelet, the "natural" way to define the analysis window should be a function of the effective wavelet within the area of interest.

Attributes computed with a fixed user-defined window will generate good images within a given target zone. In the case of laterally variable changes in layer thickness, considerable improvement can be made by adaptively defining the vertical analysis window as a function of the frequency spectrum. Laterally abrupt jumps in window radius and height are minimized by including smooth tapers along the edges. In this manner, while images at different depth may vary with data quality from high to low resolution, to significance of the anomalies will be similar.

ACKNOWLEDGEMENTS

We thank Schlumberger, for the use of the seismic data set in Westcam survey. Numerical models were generated using Tesseral's Tesseral 2D software. Seismic displays were generated used Schlumberger's Petrel software. We also thank the sponsors of Attribute-Assisted Seismic Processing and Interpretation Consortium (AASPI) for their guidance and financial support.

REFERENCES

Bahorich, M.S., and S. L. Farmer, 1995, 3-D seismic coherency for faults and stratigraphic features: The coherence cube: The Leading Edge, **14**, 1053-1058.

Barka D S., 2015, Sobel based edge detection algorithm with adaptive operator size applied to post-stack seismic data, Master thesis of University of Stavanger.

Bednar, B., 1998, Least-squares dip and coherency attributes: The Leading Edge, **17**, 777-778.

Chopra, S., and Marfurt, K. J., 2007, Seismic attributes for prospect identification and reservoir characterization. Geophysical Developments Series 11. SEG.

de Matos, D. C., and K. J. Marfurt, 2014, Complex wavelet transform spectral broadening: 84th Annual International Meeting, SEG, Extended Abstracts, 1465-1468.

Douze, E. J., and S. J. Laster, 1979, Statistics of semblance: Geophysics, **44**, 1999-2003.

Fagin, S., 1996, The fault shadow problem: Its nature and elimination: The Leading Edge, **17**, 1005-1013.

Gersztenkorn, A., and K. J. Marfurt, 1999, Eigenstructure based coherence computations as an aid to 3-D structural and stratigraphic mapping: Geophysics, **64**, 1468-1479.

Kirlin, R. L., and W. J. Done, 1999, Covariance analysis for seismic signal processing: Geophysical Developments Series, SEG**.**

Libak, A., B. Alaei and A. Torabi, 2017, Fault visualization and identification in fault seismic attribute volumes: Implications for fault geometric characterization: Interpretation, **5**(2), B1-B16.

Lin, T., B. Zhang, S. Zhan, Z. Wan, F. Li, H. Zhou, and K. J. Marfurt, 2014a, Seismic attributes of time- vs. depth-migrated data using self-adaptive window: 84th Annual International Meeting, SEG, Extended Abstracts, 1659-1662.

Lin, T., D. Chang, B. Zhang, J. Guo and K. J. Marfurt, 2014b, Seismic attributes estimation using a self-adaptive window: 84th Annual International Meeting, SEG, Extended Abstracts, 1654-1657.

Lin, T., T. Ha., K. J. Marfurt and K. Deal, 2016, Quantifying the significance of coherence anomalies: Interpretation, **4**, T205-T213.

Liu, J., and K. J. Marfurt, 2005, Matching pursuit decomposition using Morlet wavelets: 75th Annual International Meeting, SEG, Expanded Abstracts, 786-789.

Luo, Y., W. G. Higgs and W. S. Kowalik, 1996, Edge detection and stratigraphic analysis using 3D seismic data: 66th Annual International Meeting, SEG, Expanded Abstracts, 324 – 327.

Marfurt, K. J., 2006, Robust estimates of 3D reflector dip and azimuth: Geophysics, **71**, 29-40.

Marfurt, K. J., R. L. Kirlin, S. H. Farmer, and M. S. Bahorich, 1998, 3-D seismic attributes using a semblance-based coherency algorithm: Geophysics, **63**, 1150-1165.

Moser, T. J., and C. B. Howard, 2008, Diffraction imaging in depth: Geophysical Prospecting, **56**, 627-641.

Marfurt, K. J., and T. M. Alves, 2015, Pitfalls and limitations in seismic attribute interpretation of tectonic features, **3**(1), A5-A15

Neidell N. S., and M. T. Taner, 1971, Semblance and other coherency measures for multichannel data: Geophysics, **36**, 482-497.

Partyka, G., J. Gridley, and J. A. Lopez, 1999, Interpretational applications of spectral decomposition in reservoir characterization: The Leading Edge, **18**, 353-360.

Pepper, R., and G. Bejarano, 2005, Advances in seismic fault interpretation automation, AAPG Search and Discovery Article 40170, http://www.searchanddiscovery.com/documents/-2005/pepper/.

Puryear, C. I., O. N. Portniaguine, C. M. Cobos, and J. P. Castagna 2012, Constrained least-squares spectral analysis: Application to seismic data: Geophysics, **77**, V143-V167.

Van Bemmel, P. P., and R. E. F. Pepper, 2011, Seismic signal processing method and apparatus for generating a cube of variance values: US Patent, **8**, 055,026.

Walton, C., B. Evans, and M. Urosevic, 2000, Imaging coal seam structure using 3-D seismic methods: Exploration Geophysics, **31** (3), 509-514.

LIST of FIGURES

Figure 1. Vertical slices through a seismic amplitude volume co-rendered with coherence computed using a 5-trace by (a) ±0 ms, (b) ±4 ms, (c) ±20 ms, and (d) ±40 ms analysis window. Sample increment = 4 ms, bin size =12.5 m x 25 m. Note the stair-step artifacts in (a) indicated by the red circles, even for a vertical analysis window of a single sample. In this image, the stair step is due the vertical orientation of the seismic wavelet, perpendicular to the nearly horizontal reflector. (Data courtesy of NZPM).

Figure 2. The geometry of seismic migration, using the notation of the diffraction imaging community. **n** defines the normal to the hypothesized reflector at the image point. If no hypothesis is made, most algorithms assume **n** to be vertical, while some eliminate the obliquity factor completely. $\mathbf{p_s}$ and $\mathbf{p_g}$ define unit vectors at the image point. The obliquity factor is the cosine of the angle between the yellow vector and the average of the blue and red vectors.

Figure 3. (a) A simple reflectivity model showing faults with dips of 50°, 60°, 70°, and 80°. Synthetics were generated using a 2D finite difference solution of the wave equation. (b) The resulting prestack time-migrated image. Note that the seismic wavelets are perpendicular to the reflector, including near the fault edges. The images suffer from fault shadows (Fagin, 1996). Fault plane reflectors were not imaged due to the finite migration aperture of 2000 m. (c) The coherence image computed from the seismic data (b) displayed in (a) using a vertical analysis window of 1 sample. (d) The resulting prestack depth-migrated image. (e) The coherence image computed from the seismic data (d) displayed in (a) using a vertical analysis window of 1 sample. Note the

stair step artifacts are about the size of the seismic wavelet seen in (d). Depth migration has eliminated the fault shadows.

Figure 4. The diagram of the (a) fixed, small windows, (b) fixed, large window, and (c) the adaptive window tapered radially and vertically.

Figure 5. Vertical slice AA' through (a) origional seismic amplitude volume, and the seismic amplitude volume after (b) spectral balancing and (c) structural-oriented filtering. (sample interval: 4 ms).

Figure 6. The frequency spectrum of seismic amplitude volume (a) and (b) after spectral balancing.

Figure 7. Vertical slice AA' through energy ratio coherence using a constant window size of (a) $\pm$ 4 ms, (b) $\pm$ 20 ms, (c) $\pm$ 40 ms and (d) a data-adaptive window ($\pm$ 12~100 ms) of Figure 5c.

Figure 8. Zooned in section of seismic profile of Figure 5c (ranges 800~1150 ms).

Figure 9. (a) Time-structure map of Horizon A1 and (b) a horizon slice through seismic amplitude. Horizon A1 was picked as a trough.

Figure 10. Energy ratio coherence along Horizon A1 using constant window size of (a) $\pm$ 4 ms, (b) $\pm$ 20 ms, (c) $\pm$ 40 ms using 5 traces, and (d) a data-adaptive window varying between $\pm$ 12 ms and 5 traces, and $\pm$ 100 ms and 13 traces.

Figure 11. Phantom horizon 8 ms above Horizon A1 extracting along seismic amplitude data.

Figure 12. Energy ratio coherence along phantom horizon 8 ms above Horizon A1 using constant window size of (a) $\pm$ 4 ms, (b) $\pm$ 20 ms, (c) $\pm$ 40 ms using 5 traces, and (d) a

data-adaptive window varying between $\pm$ 12 ms and 5 traces, and $\pm$ 100 ms and 13 traces.

Figure 13. Phantom horizon 24 ms above Horizon A1 extracting along seismic amplitude data.

Figure 14. Energy ratio coherence along phantom horizon 24 ms above Horizon A1 using constant window size of (a) $\pm$ 4 ms, (b) $\pm$ 20 ms, (c) $\pm$ 40 ms using 5 traces, and (d) a data-adaptive window varying between $\pm$ 12 ms and 5 traces, and $\pm$ 100 ms and 13 traces.

Figure 15. Phantom horizon 40 ms above Horizon A1 extracting along seismic amplitude data.

Figure 16. Energy ratio coherence along phantom horizon 40ms above Horizon A1 using constant window size of (a) $\pm$ 4 ms, (b) $\pm$ 20 ms, (c) $\pm$ 40 ms using 5 traces, and (d) a data-adaptive window varying between $\pm$ 12 ms and 5 traces, and $\pm$ 100 ms and 13 traces.

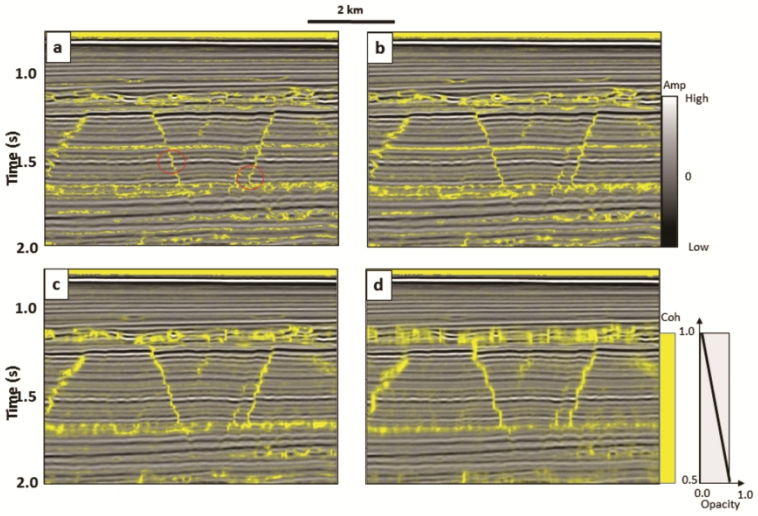

Figure 1. Vertical slices through a seismic amplitude volume co-rendered with coherence computed using a 5-trace by (a) ±0 ms, (b) ±4 ms, (c) ±20 ms, and (d) ±40 ms analysis window. Sample increment = 4 ms, bin size =12.5 m x 25 m. Note the stair-step artifacts in (a) indicated by the red circles, even for a vertical analysis window of a single sample. In this image, the stair step is due the vertical orientation of the seismic wavelet, perpendicular to the nearly horizontal reflector. (Data courtesy of NZPM).

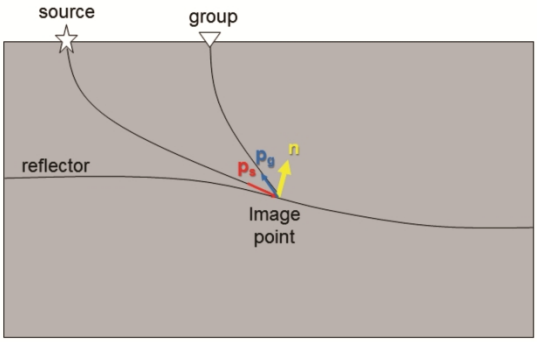

Figure 2. The geometry of seismic migration, using the notation of the diffraction imaging community. n defines the normal to the hypothesized reflector at the image point. If no hypothesis is made, most algorithms assume n to be vertical, while some eliminate the obliquity factor completely. ps and pg define unit vectors at the image point. The obliquity factor is the cosine of the angle between the yellow vector and the average of the blue and red vectors.

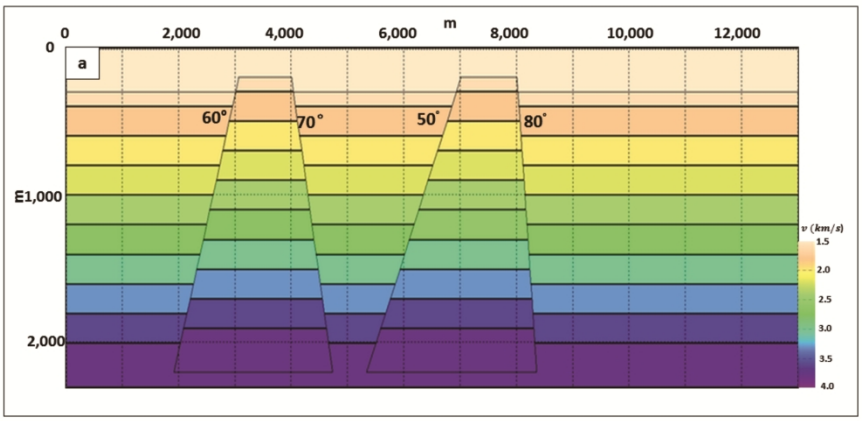

Figure 3a. (a) A simple reflectivity model showing faults with dips of 50°, 60°, 70°, and 80°. Synthetics were generated using a 2D finite difference solution of the wave equation. (b) The resulting prestack time-migrated image. Note that the seismic wavelets are perpendicular to the reflector, including near the fault edges. The images suffer from fault shadows (Fagin, 1996). Fault plane reflectors were not imaged due to the finite migration aperture of 2000 m. (c) The coherence image computed from the seismic data (b) displayed in (a) using a vertical analysis window of 1 sample. (d) The resulting prestack depth-migrated image. (e) The coherence image computed from the seismic data (d) displayed in (a) using a vertical analysis window of 1 sample. Note the
stair step artifacts are about the size of the seismic wavelet seen in (d). Depth migration has eliminated the fault shadows.

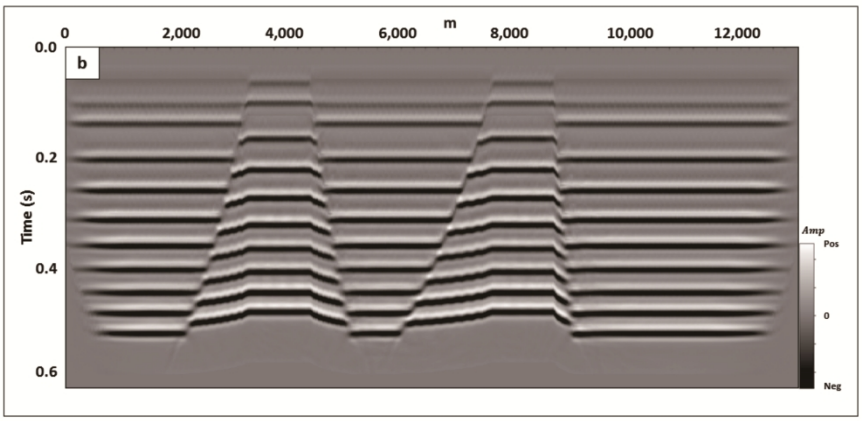

Figure 3b. (a) A simple reflectivity model showing faults with dips of 50°, 60°, 70°, and 80°. Synthetics were generated using a 2D finite difference solution of the wave equation. (b) The resulting prestack time-migrated image. Note that the seismic wavelets are perpendicular to the reflector, including near the fault edges. The images suffer from fault shadows (Fagin, 1996). Fault plane reflectors were not imaged due to the finite migration aperture of 2000 m. (c) The coherence image computed from the seismic data (b) displayed in (a) using a vertical analysis window of 1 sample. (d) The resulting prestack depth-migrated image. (e) The coherence image computed from the seismic data (d) displayed in (a) using a vertical analysis window of 1 sample. Note the
stair step artifacts are about the size of the seismic wavelet seen in (d). Depth migration has eliminated the fault shadows.

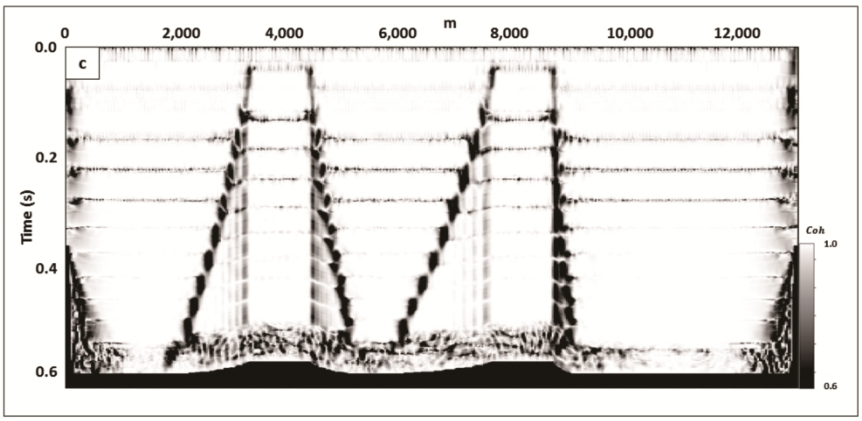

Figure 3c. (a) A simple reflectivity model showing faults with dips of 50°, 60°, 70°, and 80°. Synthetics were generated using a 2D finite difference solution of the wave equation. (b) The resulting prestack time-migrated image. Note that the seismic wavelets are perpendicular to the reflector, including near the fault edges. The images suffer from fault shadows (Fagin, 1996). Fault plane reflectors were not imaged due to the finite migration aperture of 2000 m. (c) The coherence image computed from the seismic data (b) displayed in (a) using a vertical analysis window of 1 sample. (d) The resulting prestack depth-migrated image. (e) The coherence image computed from the seismic data (d) displayed in (a) using a vertical analysis window of 1 sample. Note the
stair step artifacts are about the size of the seismic wavelet seen in (d). Depth migration has eliminated the fault shadows.

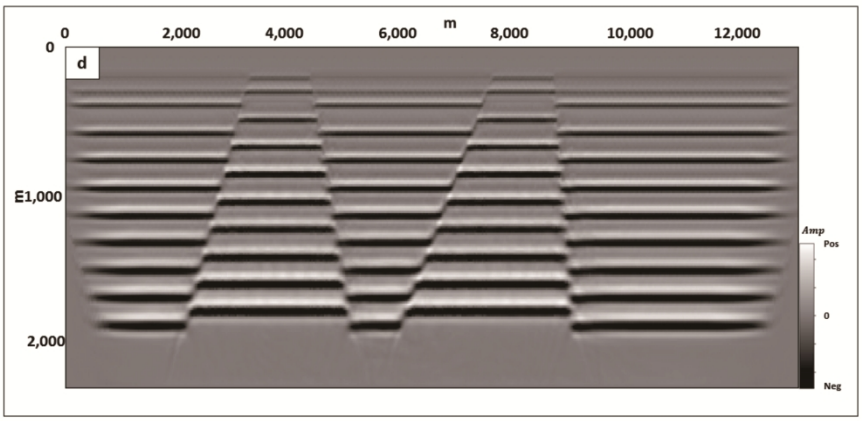

Figure 3d. (a) A simple reflectivity model showing faults with dips of 50°, 60°, 70°, and 80°. Synthetics were generated using a 2D finite difference solution of the wave equation. (b) The resulting prestack time-migrated image. Note that the seismic wavelets are perpendicular to the reflector, including near the fault edges. The images suffer from fault shadows (Fagin, 1996). Fault plane reflectors were not imaged due to the finite migration aperture of 2000 m. (c) The coherence image computed from the seismic data (b) displayed in (a) using a vertical analysis window of 1 sample. (d) The resulting prestack depth-migrated image. (e) The coherence image computed from the seismic data (d) displayed in (a) using a vertical analysis window of 1 sample. Note the
stair step artifacts are about the size of the seismic wavelet seen in (d). Depth migration has eliminated the fault shadows.

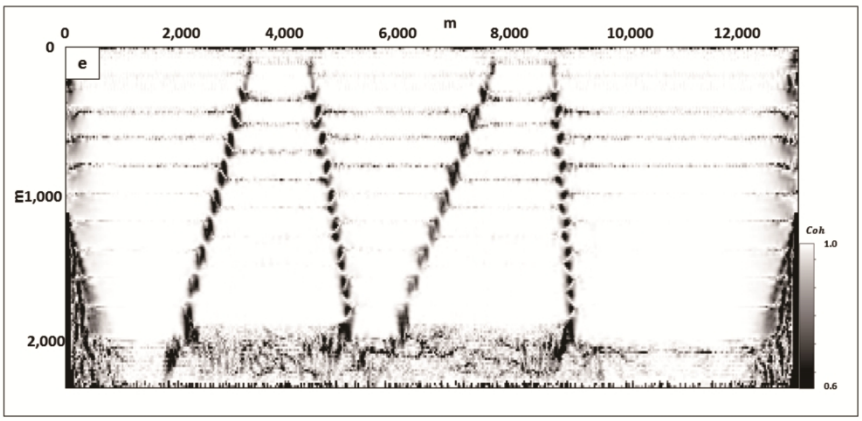

Figure 3e. (a) A simple reflectivity model showing faults with dips of 50°, 60°, 70°, and 80°. Synthetics were generated using a 2D finite difference solution of the wave equation. (b) The resulting prestack time-migrated image. Note that the seismic wavelets are perpendicular to the reflector, including near the fault edges. The images suffer from fault shadows (Fagin, 1996). Fault plane reflectors were not imaged due to the finite migration aperture of 2000 m. (c) The coherence image computed from the seismic data (b) displayed in (a) using a vertical analysis window of 1 sample. (d) The resulting prestack depth-migrated image. (e) The coherence image computed from the seismic data (d) displayed in (a) using a vertical analysis window of 1 sample. Note the
stair step artifacts are about the size of the seismic wavelet seen in (d). Depth migration has eliminated the fault shadows.

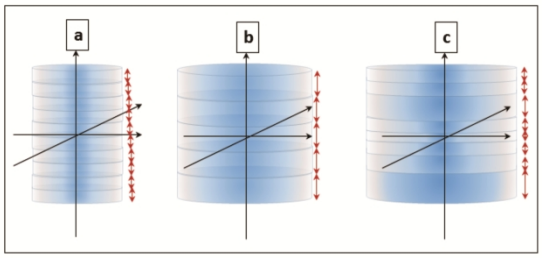

Figure 4. The diagram of the (a) fixed, small windows, (b) fixed, large window, and (c) the adaptive window tapered radially and vertically.

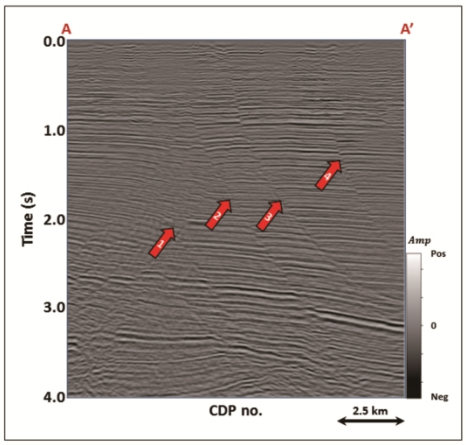

Figure 5a. Vertical slice AA' through (a) origional seismic amplitude volume, and the seismic amplitude volume after (b) spectral balancing and (c) structural-oriented filtering. (sample interval: 4 ms).

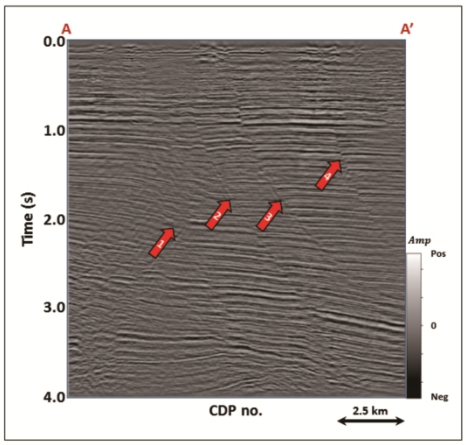

Figure 5b. Vertical slice AA' through (a) origional seismic amplitude volume, and the seismic amplitude volume after (b) spectral balancing and (c) structural-oriented filtering. (sample interval: 4 ms).

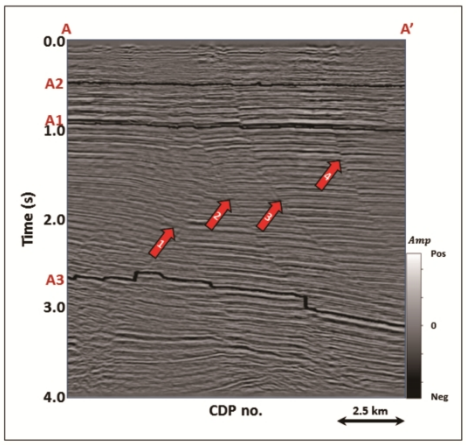

Figure 5c. Vertical slice AA' through (a) origional seismic amplitude volume, and the seismic amplitude volume after (b) spectral balancing and (c) structural-oriented filtering. (sample interval: 4 ms).

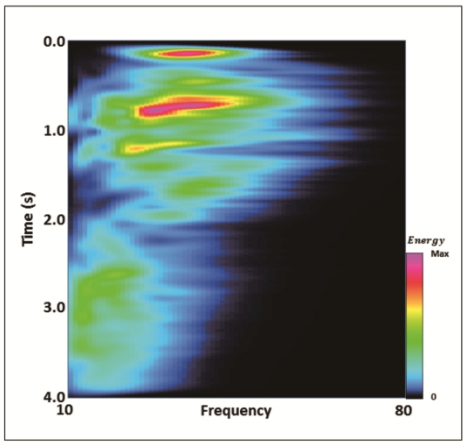

Figure 6a. The frequency spectrum of seismic amplitude volume (a) and (b) after spectral balancing.

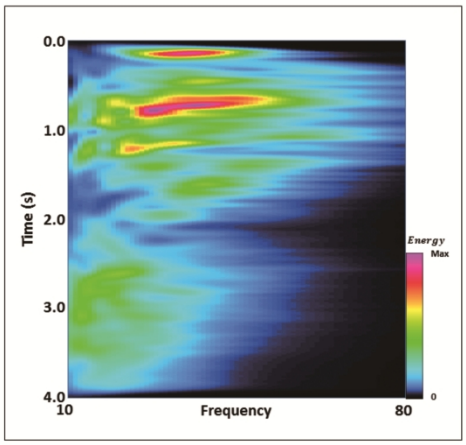

Figure 6b. The frequency spectrum of seismic amplitude volume (a) and (b) after spectral balancing.

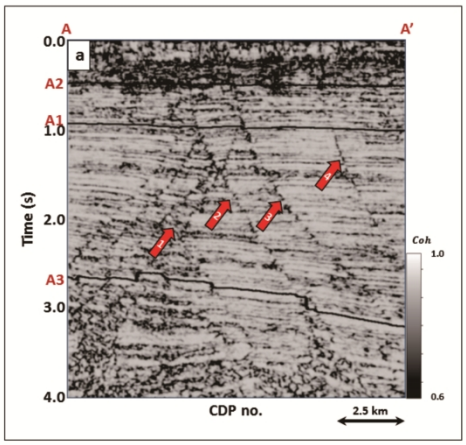

Figure 7a. Vertical slice AA' through energy ratio coherence using a constant window size of (a) ±4 ms, (b) ±20 ms, (c) ±40 ms and (d) a data-adaptive window (±12~100 ms) of Figure 5c.

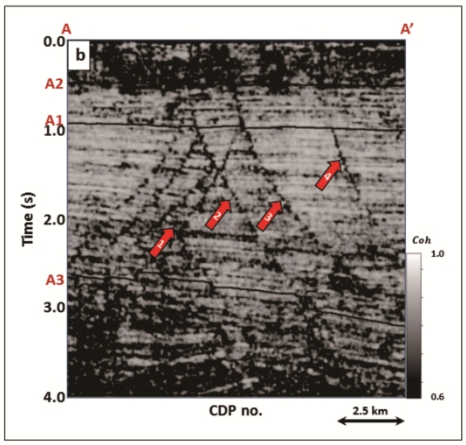

Figure 7b. Vertical slice AA' through energy ratio coherence using a constant window size of (a) ±4 ms, (b) ±20 ms, (c) ±40 ms and (d) a data-adaptive window (±12~100 ms) of Figure 5c.

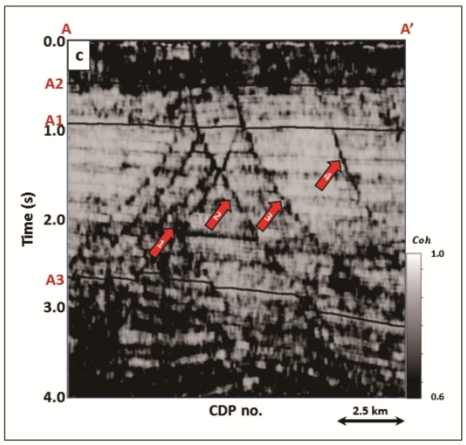

Figure 7c. Vertical slice AA' through energy ratio coherence using a constant window size of (a) ±4 ms, (b) ±20 ms, (c) ±40 ms and (d) a data-adaptive window (±12~100 ms) of Figure 5c.

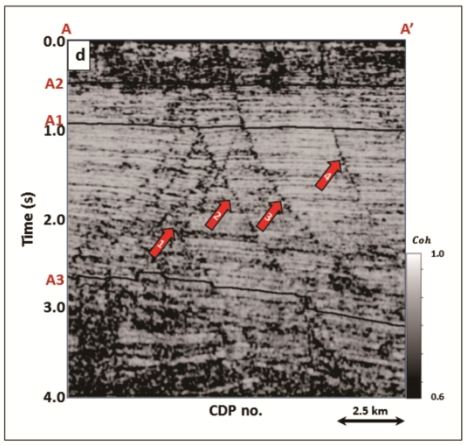

Figure 7d. Vertical slice AA' through energy ratio coherence using a constant window size of (a) ±4 ms, (b) ±20 ms, (c) ±40 ms and (d) a data-adaptive window (±12~100 ms) of Figure 5c.

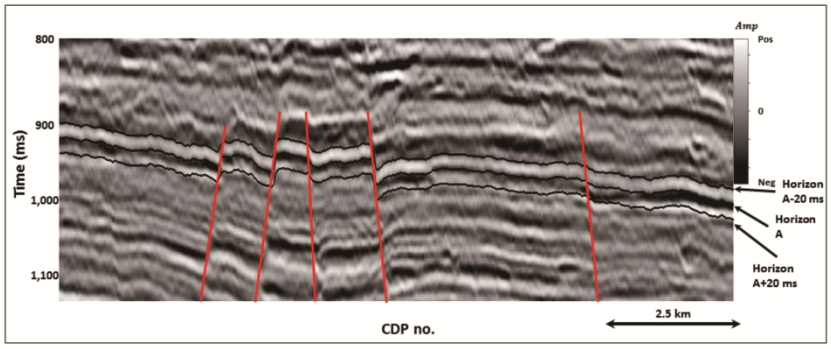

Figure 8. Zooned in section of seismic profile of Figure 5c (ranges 800~1150 ms).

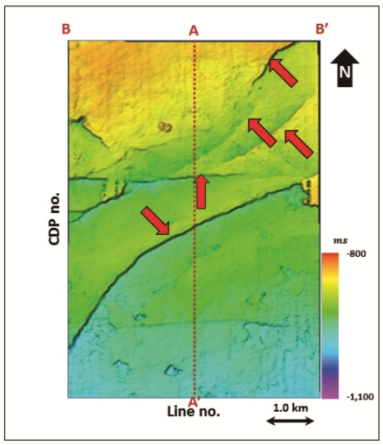

Figure 9a. (a) Time-structure map of Horizon A1 and (b) a horizon slice through seismic amplitude. Horizon A1 was picked as a trough.

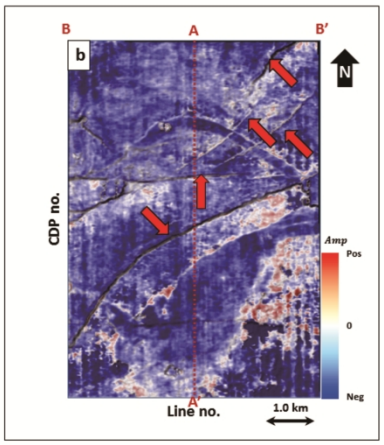

Figure 9b. (a) Time-structure map of Horizon A1 and (b) a horizon slice through seismic amplitude. Horizon A1 was picked as a trough.

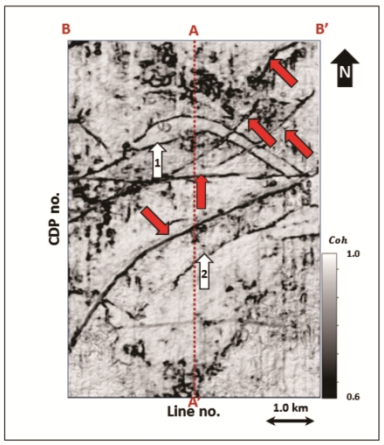

Figure 10a. Energy ratio coherence along Horizon A1 using constant window size of (a) ±4 ms, (b) ±20 ms, (c) ±40 ms using 5 traces, and (d) a data-adaptive window varying between ±12 ms and 5 traces, and ±100 ms and 13 traces.

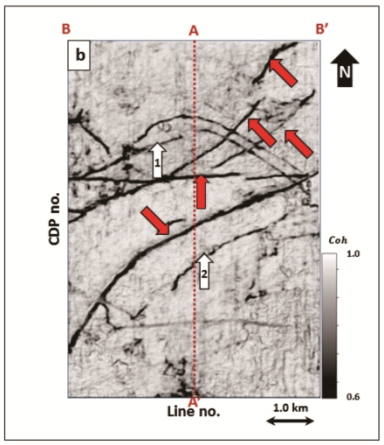

Figure 10b. Energy ratio coherence along Horizon A1 using constant window size of (a) ±4 ms, (b) ±20 ms, (c) ±40 ms using 5 traces, and (d) a data-adaptive window varying between ±12 ms and 5 traces, and ±100 ms and 13 traces.

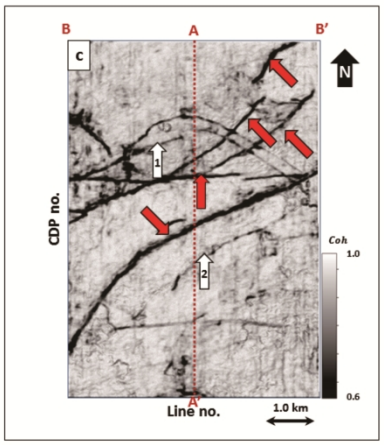

Figure 10c. Energy ratio coherence along Horizon A1 using constant window size of (a) ±4 ms, (b) ±20 ms, (c) ±40 ms using 5 traces, and (d) a data-adaptive window varying between ±12 ms and 5 traces, and ±100 ms and 13 traces.

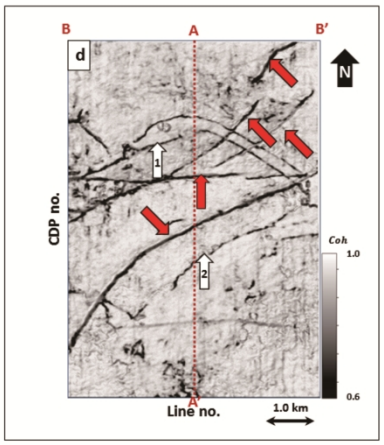

Figure 10d. Energy ratio coherence along Horizon A1 using constant window size of (a) ±4 ms, (b) ±20 ms, (c) ±40 ms using 5 traces, and (d) a data-adaptive window varying between ±12 ms and 5 traces, and ±100 ms and 13 traces.

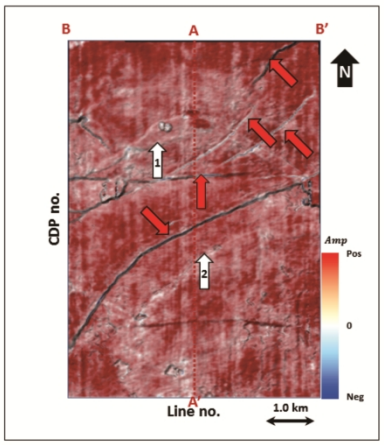

Figure 11. Phantom horizon 8 ms above Horizon A1 extracting along seismic amplitude data.

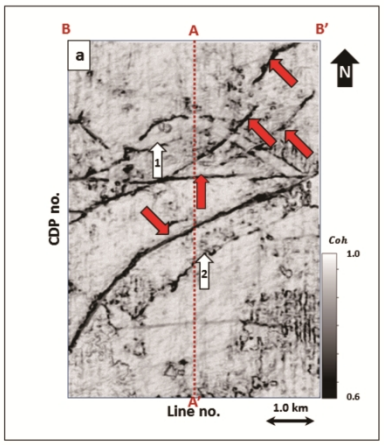

Figure 12a. Energy ratio coherence along phantom horizon 8 ms above Horizon A1 using constant window size of (a) ±4 ms, (b) ±20 ms, (c) ±40 ms using 5 traces, and (d) a data-adaptive window varying between ±12 ms and 5 traces, and ±100 ms and 13 traces.

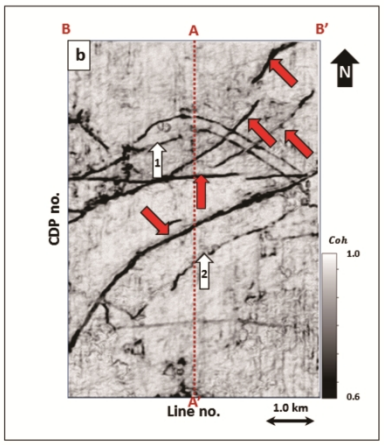

Figure 12b. Energy ratio coherence along phantom horizon 8 ms above Horizon A1 using constant window size of (a) ±4 ms, (b) ±20 ms, (c) ±40 ms using 5 traces, and (d) a data-adaptive window varying between ±12 ms and 5 traces, and ±100 ms and 13 traces.

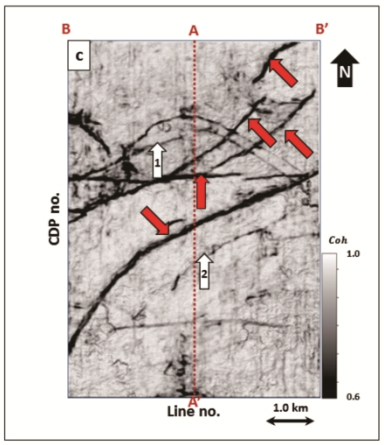

Figure 12c. Energy ratio coherence along phantom horizon 8 ms above Horizon A1 using constant window size of (a) ±4 ms, (b) ±20 ms, (c) ±40 ms using 5 traces, and (d) a data-adaptive window varying between ±12 ms and 5 traces, and ±100 ms and 13 traces.

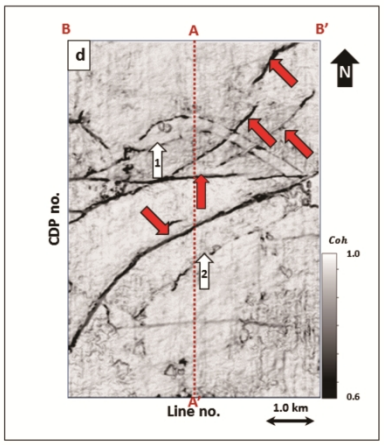

Figure 12d. Energy ratio coherence along phantom horizon 8 ms above Horizon A1 using constant window size of (a) ±4 ms, (b) ±20 ms, (c) ±40 ms using 5 traces, and (d) a data-adaptive window varying between ±12 ms and 5 traces, and ±100 ms and 13 traces.

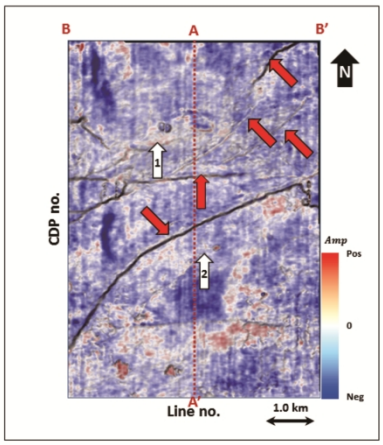

Figure 13. Phantom horizon 24 ms above Horizon A1 extracting along seismic amplitude data.

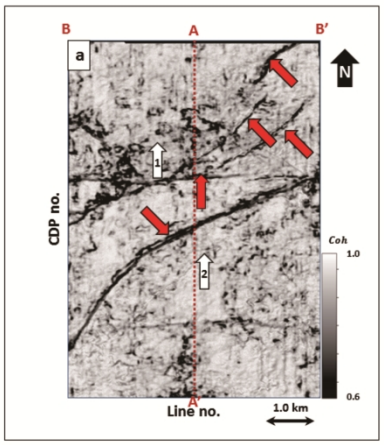

Figure 14a. Energy ratio coherence along phantom horizon 24 ms above Horizon A1 using constant window size of (a) ±4 ms, (b) ±20 ms, (c) ±40 ms using 5 traces, and (d) a data-adaptive window varying between ±12 ms and 5 traces, and ±100 ms and 13 traces.

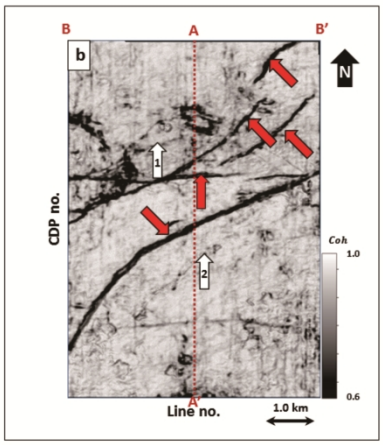

Figure 14b. Energy ratio coherence along phantom horizon 24 ms above Horizon A1 using constant window size of (a) ±4 ms, (b) ±20 ms, (c) ±40 ms using 5 traces, and (d) a data-adaptive window varying between ±12 ms and 5 traces, and ±100 ms and 13 traces.

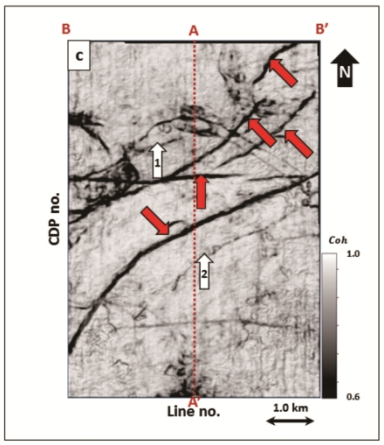

Figure 14c. Energy ratio coherence along phantom horizon 24 ms above Horizon A1 using constant window size of (a) ±4 ms, (b) ±20 ms, (c) ±40 ms using 5 traces, and (d) a data-adaptive window varying between ±12 ms and 5 traces, and ±100 ms and 13 traces.

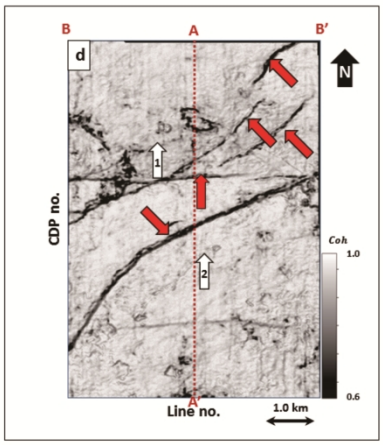

Figure 14d. Energy ratio coherence along phantom horizon 24 ms above Horizon A1 using constant window size of (a) ±4 ms, (b) ±20 ms, (c) ±40 ms using 5 traces, and (d) a data-adaptive window varying between ±12 ms and 5 traces, and ±100 ms and 13 traces.

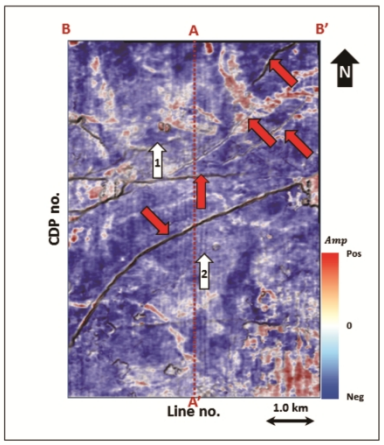

Figure 15. Phantom horizon 40 ms above Horizon A1 extracting along seismic amplitude data.

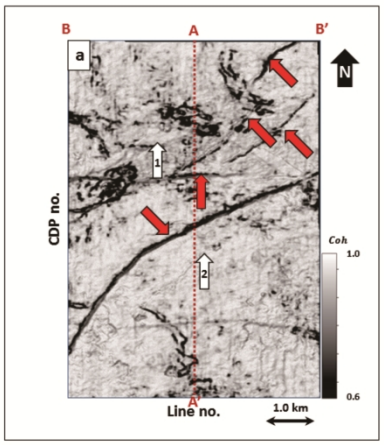

Figure 16a. Energy ratio coherence along phantom horizon 40ms above Horizon A1 using constant window size of (a) ±4 ms, (b) ±20 ms, (c) ±40 ms using 5 traces, and (d) a data-adaptive window varying between ±12 ms and 5 traces, and ±100 ms and 13 traces.

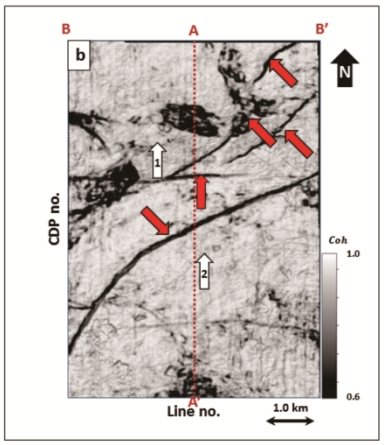

Figure 16b. Energy ratio coherence along phantom horizon 40ms above Horizon A1 using constant window size of (a) ±4 ms, (b) ±20 ms, (c) ±40 ms using 5 traces, and (d) a data-adaptive window varying between ±12 ms and 5 traces, and ±100 ms and 13 traces.

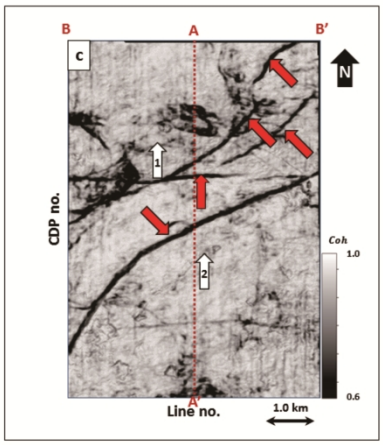

Figure 16c. Energy ratio coherence along phantom horizon 40ms above Horizon A1 using constant window size of (a) ±4 ms, (b) ±20 ms, (c) ±40 ms using 5 traces, and (d) a data-adaptive window varying between ±12 ms and 5 traces, and ±100 ms and 13 traces.

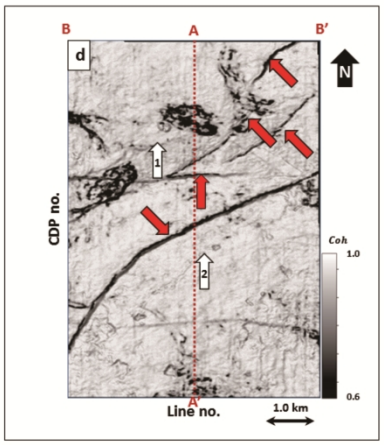

Figure 16d. Energy ratio coherence along phantom horizon 40ms above Horizon A1 using constant window size of (a) ±4 ms, (b) ±20 ms, (c) ±40 ms using 5 traces, and (d) a data-adaptive window varying between ±12 ms and 5 traces, and ±100 ms and 13 traces.

DATA AND MATERIALS AVAILABILITY

Data associated with this research are available and can be obtained by contacting the corresponding author.